Energy Storage Materials 18 (2019) 366–374

Contents lists available at ScienceDirect

Energy Storage Materials

journal homepage: www.elsevier.com/locate/ensm

Tin sulfide nanoparticles embedded in sulfur and nitrogen dual-doped mesoporous carbon fibers as high-performance anodes with battery-capacitive sodium storage

Yaping Wang[a,b,1], Yifang Zhang[a,c,1], Junrong Shi[a], Xiangzhong Kong[a], Xinxin Cao[a], Shuquan Liang[a,*], Guozhong Cao[a,d], Anqiang Pan[a,*]

[a] School of Materials Science & Engineering, Central South University, Changsha 410083, Hunan, China
[b] Light Alloy Research Institute, Central South University, Changsha 410083, Hunan, China
[c] Department of Chemistry and Energy Sciences Institute, Yale University, West Haven, CT 06516, USA
[d] Department of Materials Science & Engineering, University of Washington, Seattle, WA 98195, USA

ARTICLE INFO

Keywords:
SnS
Carbon fibers
Sulfur/nitrogen-doped carbon
Sodium-ion batteries
Capacitive effect

ABSTRACT

Batteries based on sodium-ion chemistry are promising alternatives to current-generation lithium-ion ones, owing to the abundant sodium sources. The larger radius of Na^+ than Li^+, however, has been limiting the adaptability of many electrode materials. On one hand, the insertion of Na^+ harshly requires suitable layer spacing. On the other hand, the sodiation/desodiation may cause more severe volume changes. Herein, nanosized tin sulfide embedded in sulfur and nitrogen co-doped porous carbon fibers (SnS@SNCF) were designed and synthesized from a sulfur bearing electrospinning solution. This approach promises the structural stability of SnS upon cycling to ensure high capacities. Meanwhile, it introduces sulfur doping, pores and partially graphitized edges to the carbon fibers, which can contribute to fast capacitive sodium storage. An optimized SnS@SNCF electrode shows high specific capacity of 630 mA h g^{-1} at 0.1 A g^{-1}, good rate capability and superior cyclic stability in half-cell. It also shows potential in SnS@SNCF//$Na_3V_2(PO_4)_3$ full cells.

1. Introduction

Sodium-ion batteries (SIBs) are promising candidates for low-cost and large-scale energy storage and conversion systems because of the natural abundance of sodium [1–4]. The electrode materials, especially anode materials, are one of the major dilemmas that have hampered SIBs into practical application. Unlike the commercialized lithium-ion batteries (LIBs), the larger size of Na^+ (1.02 Å) than Li^+ (0.76 Å) has put the sodium-ion-based chemistry in dire straits [5,6].

Commercial graphite anode for LIBs cannot store sodium *via* the insertion/extraction mechanism in carbonate electrolyte [2,4,7]. Hard carbon, as a promising SIB anode that lifts the limitation of graphite, still suffers from finite capacity (~ 300 mA h g^{-1}) and low Coulombic efficiency [7]. Metal-based (oxide [8,9], sulfide [10,11] or alloy [12,13]) anodes that storage sodium *via* conversion or alloying-dealloying mechanism have much higher theoretical capacity, among which metal sulfide is a potential class of SIB anode materials with high electronic and ionic conductivity [10]. Moreover, compared with metal oxides, metal sulfides are typically more reversible owing to the relatively weaker M-S bonds than M-O bonds (M = metal), which can contribute to high Coulombic efficiency. Of all metal sulfides, SnS stands out for hosting Na^+ because of its unique layered structure and large interlayer spacing [14–16]. After the conversion reaction to form metallic tin dispersed in Na_2S matrix [17], the alloying of tin with sodium can further release capacity. However, in sodium-ion-based chemistry, the reaction of host materials with sodium may experience more severe volume expansion and structural distortion. For example, 424% volume expansion would take place from Sn to $Na_{15}Sn_4$ with 847 mA h g^{-1} of capacity delivered, while only 250% expansion is expected from Sn to $Li_{22}Sn_5$ with higher specific capacity of 992 mA h g^{-1}. The large volume expansion may lead to continuous pulverization and deteriorate the cycling stability [13,18,19].

One solution to address these issues is to prepare electrode materials with smaller particle size. To prevent active materials from aggregation and buffer the volume change, dispersing nanoparticles in a conducting skeleton has been mostly used [20,21]. Electrospinning is a facile and effective way to fabricate well-dispersed nanoparticles in conductive carbon fibers [22,23]. However, the introduction of carbon

* Corresponding authors.
E-mail addresses: lsq@csu.edu.cn (S. Liang), pananqiang@csu.edu.cn (A. Pan).
[1] The authors are contributed equally to this work.

https://doi.org/10.1016/j.ensm.2018.08.014
Received 14 June 2018; Received in revised form 3 August 2018; Accepted 15 August 2018
Available online 18 August 2018
2405-8297/

skeleton may constrain the overall capacity. Literatures have reported the surface adsorption sodium storage of carbon materials, which is based on capacitive mechanism with high kinetics [24]. Porous carbon skeleton with high surface area is desired in term of increasing the capacitive capacity. In addition, heteroatom (such as sulfur, nitrogen, boron and phosphorus) doping has recently emerged as an effective method to enhance the physical and chemical properties of carbonaceous materials [24,25]. The incorporation of heteroatoms can enhance electronic conductivity to accelerate electron transport, enlarge specific surface area and increase active sites for Na^+ adsorption. Furthermore, compared with unitary-heteroatom doping, binary-heteroatom doping can obtain higher electronic conductivity and larger interlayer distance due to the synergistic effect of two elements [26–28].

Herein, we report the *in-situ* fabrication of SnS nanoparticles encapsulated in sulfur and nitrogen duo-doped porous carbon fibers (SnS@SNCF) using an electrospinning technique and subsequent thermal treatments. A unique sulfur bearing solution was first prepared to make sulfur spinnable, in which way sulfur can provide source for SnS, induce pores and create S-doping in carbon during the annealing process. The nano-sized SnS, as battery-type active materials, is uniformly dispersed in carbon matrix, which can ensure short ion diffusion paths, buffer volume changes and inhibit aggregations. The heteroatom-doped porous carbon can provide abundant active sites for fast capacitive sodium storage, which contributes greatly to high rate capability. The battery-capacitive synchronous sodium storage of SnS@SNCF leads to superior electrochemical performance, with high specific capacity of 630 mA h g^{-1} at 0.1 A g^{-1} delivered in half cell and promising potentials in full cells.

2. Experimental section

2.1. Synthesis of SnS@sulfur and nitrogen doped carbon fibers (SnS@SNCF)

All chemical reagents and solvents were used as received without further purification. In an optimized synthesis, 0.625 g of $SnCl_2{\cdot}2H_2O$ and 0.5 g of polyacrylonitrile (PAN, M_w = 1,500,000) were dissolved in 6 mL of *N*, *N*-Dimethylformamide (DMF). Sulfur powder with S:Sn = 2:1 (molar ratio) was added into the above solution with further stirring at 80 °C for 12 h to form a yellowish transparent solution. In the electrospinning process, the obtained mixed viscous solution was inhaled into a syringe with a stainless steel nozzle (0.58 mm of inner diameter). The flow rate of the solution was set to be 10 μL min^{-1} and a grounded stainless steel plate was placed 15 cm below the needle to collect the spinning fiber. A voltage of 10 kV was applied between the needle and the plate to initiate the electrospinning. The as-collected fibers were first stabilized in air at 250 °C for 40 min with a heating rate of 2 °C min^{-1}. Then, the fibers were carbonized in a tube furnace at 600 °C for 2 h under Ar atmosphere with the same ramping rate to obtain the final SnS@SNCF product. The contents of SnS and carbon in the SnS@SNCF were tuned by adding different amount of $SnCl_2{\cdot}2H_2O$ (0.25, 0.5, 0.625, or 0.75 g) and corresponding S powder in the electrospinning solution (0.5 g of PAN, 6 mL of DMF) to study their influences on the morphologies and properties of products. For comparison, SnS and carbon composite (SnS-C) was prepared by evaporating DMF in the electrospinning solution (with 0.625 g of $SnCl_2{\cdot}2H_2O$ and corresponding sulfur being added), followed by annealing the mixture in Ar atmosphere at 600 °C for 2 h. Bare SnS was also prepared by a similar process without adding PAN in the DMF solution. Other metal (cobalt, nickel, copper and zinc) chlorides were also used to study the dissolution ability of sulfur in the electrospinning solution.

2.2. Materials characterization

The X-ray diffraction (XRD) patterns were collected using a Rigaku D/max 2500 with Cu-Kα radiation (λ = 1.54178 Å) in the range between 10° and 80° (2θ) with a step size of 0.02°. The morphologies and interior structures of the samples were characterized by scanning electron microscopy (SEM, Quanta FEG 250) and transmission electron microscopy (TEM, JEOL JEM-2100F). Thermogravimetric analysis (TGA) was conducted on NETZSCH STA 449 C. X-ray photoelectron spectroscopy (XPS) was performed on ESCALAB 250Xi (ThermoFisher-VG Scientific, Britain). Raman spectroscopy measurements were performed at room temperature in a spectrometer (LabRAM Hr800) with a back-illuminated charge coupled detector (CCD) attachment.

2.3. Electrochemical measurement

The electrochemical measurements were carried out using CR2016 coin-type cells with 1.0 M $NaClO_4$ in propylene carbonate (PC) with 5% fluoroethylene carbonate (FEC) as electrolyte, and glass microfiber (Whatman, GF/D) as separator. In half cell, Na sheets were used as counter electrode. The working electrode was prepared by mixing the as-prepared active materials, super-p and sodium carboxymethyl cellulose (CMC) in a weight ratio of 70:15:15 in deionized water to make slurry. The slurry was coated on copper foils and dried in a vacuum oven at 80 °C for 12 h. In full cell, $Na_3V_2(PO_4)_3$ was used as cathode electrode materials. The electrode was prepared by mixing $Na_3V_2(PO_4)_3$, super-p and CMC in a weight ratio of 75:15:10 in deionized water and then coated onto an aluminum foil and dried at 80 °C for 12 h. The full-cell was assembled based on the capacity ratio of ≈ 1.2:1 between cathode and the SnS@SNCF anode. A presodiation procedure was carried out for SnS@SNCF by applying three-times of discharge-charge cycles in half cells before assembling into full cells. Cyclic voltammetry was tested with an electrochemical workstation (CHI660C). The galvanostatic charge/discharge performances of the electrodes were conducted on a Land battery tester (Land CT 2001A, Wuhan, China).

3. Results and discussion

Fig. 1 illustrates the fabrication of SnS nanoparticles embedded in S and N dual-doped mesoporous carbon fibers (SnS@SNCF). A sulfur bearing electrospinning solution was obtained by adding sulfur powder, stannous chloride, and polyacrylonitrile (PAN) in *N*, *N*-Dimethylformamide (DMF) at 80 °C (Step I). It can be seen that sulfur exists in solid state in DMF. However, by adding tin ions, a yellowish solution was obtained, which made sulfur spinnable. Other metal chlorides were also applied to dissolve sulfur in the electrospinning solution. While none of cobalt, nickel, copper, or zinc chloride can help as much as tin (Fig. S1). Sulfur may exist as homocyclic sulfuroxide complexed with stannous chloride to form an adduct in the DMF solution [29], as indicated by the major XRD peaks of the product after evaporating DMF (Fig. S2). These results demonstrate the unique method towards a sulfur bearing electrospinning solution with the assistance of stannous chloride.

The precursor solution was then electrospun into fibers (Step II, Fig. 1). A stabilization step was conducted for the cyclization of PAN into conjugated structure (Step III) [30]. During this process, tin and sulfur species reacted to form SnS_2 encapsulated in the fibers (XRD patterns, Fig. S3). Afterwards, the fibers were annealed in Ar atmosphere at 600 °C (Step IV). By adding a proper amount of sulfur and tin source in the PAN-based spinning solution, the fibers can be tuned to be porous while maintaining the integrity of the fibrous structure. As shown in Fig. 1c, SnS nanoparticles are well dispersed in the carbon fiber matrix, which can effectively mitigate the strain formed during sodiation/desodiation, shorten the pathways for ionic diffusion and charge transfer, as well as avoiding the aggregation of SnS particles during cycling. In addition, the fibers are sulfur and nitrogen duo-doped with partially graphitized edges, which provides abundant active sites for fast capacitive sodium-storage and guarantees fast electron transportations.

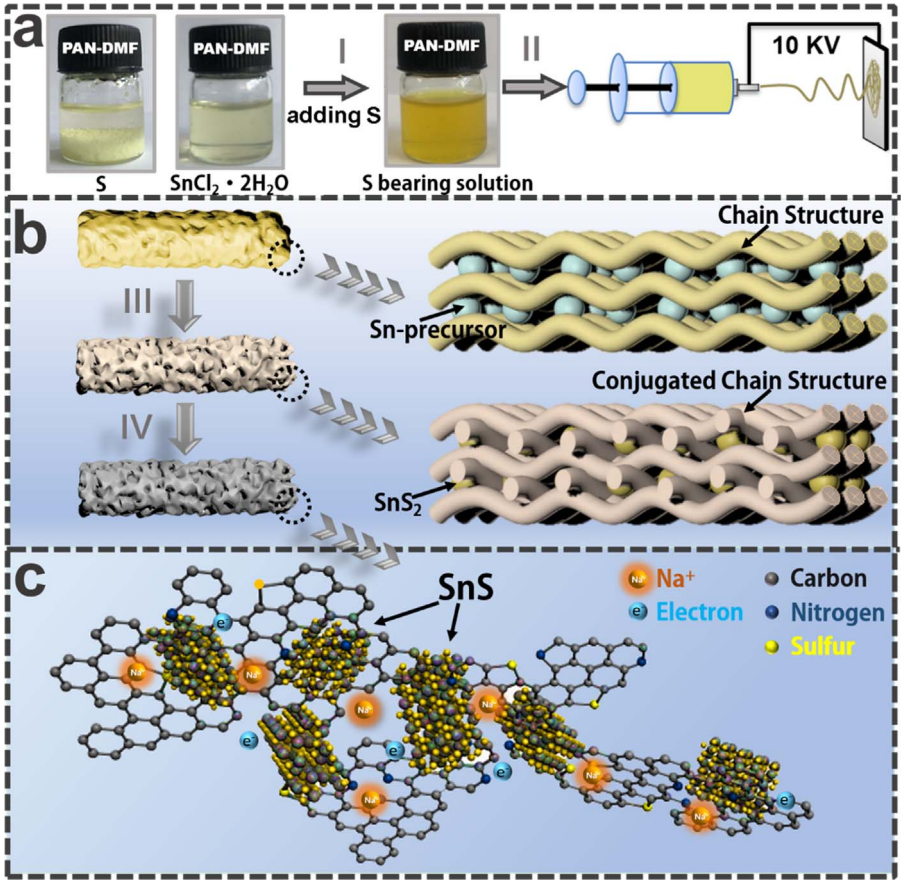

Fig. 1. Schematic illustration of the synthesis of a sulfur bearing electrospinning solution (a), tin sulfide embedded in conjugated and carbonized PAN (b), and fast battery-capacitive sodium storage (c).

To enhance the overall capacity of SnS@SNCF, a higher content of SnS was desired. Different amounts of tin chloride and sulfur reagents (Sn:S with molar ratios of 1:2) were added when preparing the PAN-based spinning solution. As shown in Fig. S4, the XRD patterns of all the annealed products can be identified as orthorhombic SnS (JCPDS card No. 73-1859: *Pnma (62)*, a = 11.18 Å, b = 3.982 Å, c = 4.329 Å). However, a bulged peak at around 26° can be observed when only 0.25 g of $SnCl_2{\cdot}2H_2O$ and corresponding S were added, which can be ascribed to carbon. The bulged peak becomes weaker as the content of reagent increases. The fibers are with smooth surface when the content of reagent is low (Fig. S5a, b). The surfaces become rough while the fibrous structures remain integrity as the $SnCl_2{\cdot}2H_2O$ reagent increases to 0.5 and 0.625 g (Fig. S5c, d and Fig. 2). Further increasing the reagent content will lead to serious agglomeration with ~ 40 μm large bulks twined with fibers. (Fig. S5e, f), showing that the low content of PAN cannot guarantee a stable skeleton to support tin and sulfur species. The SnS content in the SnS@SNCF was tested and calculated according to the TG result (Fig. S6), which is 38.3%, 48.5%, 55.6% or 65.1% when 0.25, 0.5, 0.625 or 0.75 g of $SnCl_2{\cdot}2H_2O$ was added in 6 mL of spinning solution. The SnS@SNCF products were then denoted as SnS@SNCF-38, SnS@SNCF-48, SnS@SNCF-55 and SnS@SNCF-65, respectively.

The morphology and structure of the SnS@SNCF-55 sample was further observed in detail. The SEM image Fig. 2a displays the SnS@SNCF-55 with continuous and uniform fibrous morphology. The high magnification SEM image (Fig. 2b) shows the fibers are 1 μm in diameter with sheet-like rough surface. This construction inherits the structure of the precursor fibers and the products after stabilization in air (Fig. S7, S8), which may result from the released gas due to the partial sublimation and oxidation of sulfur under high voltage during the electrospinning and the annealing process. The TEM image (Fig. 2c, d) further demonstrates the fibers with porous structure constructed by nanosheets. As determined by N_2 sorption measurement (Fig. S9), SnS@SNCF-55 possess a relatively high Brunauer–Emmett–Teller (BET) surface area of 50.7 $m^2\ g^{-1}$ with pore sizes mostly below 10 nm. The porous construction can provide penetrable channels for electrolytes and reduce the migration paths for sodium ions. In the HRTEM image Fig. 2e that taken from a thin sheet, well-dispersed SnS nanoparticles can be found in the carbon matrix. Lattice fringes with d-spacings of 0.3422 and 0.2348 nm are detected, corresponding to the planar distances of (201) and (401) planes of SnS, respectively. In Fig. 2f, the selected-area electron diffraction (SAED) patterns indicate the polycrystalline feature of SnS, and the intense rings can be assigned to (400) (410) (502) and (811) crystal planes, respectively. Besides, the edges of carbon fiber are partly graphitized with interlayer distance of 0.39 nm (insets of Fig. 2g). The enlarged interlayer distances comparing with graphite (0.335 nm) [31,32] can be attributed to the S/N co-doping, which is beneficial for the insertion/extraction or adsorption/desorption of Na-ion [24,26,33]. The elemental mapping results (Fig. 2h–l) reveal the homogeneous distribution of Sn, S, C and N elements in the SnS@SNCF-55 sample, further verifying the SnS nanoparticles are well dispersed in the S and N co-doped carbon fibers. For comparison, bare SnS was prepared by dissolving sulfur and $SnCl_2{\cdot}2H_2O$ in DMF, evaporating DMF, and annealing the remaining mixture. The mixture is composed of particles with size of ~ 2 μm (Fig. S10). After the annealing process, pure SnS phase can be obtained (Fig. S11a). However, the morphologies of SnS are ~ 2 μm thick plates (Fig. S11b), suggesting the agglomeration of SnS during calcination can be effectively suppressed by the confinement of carbon fibers. A SnS-C composite was also prepared by annealing the mixture after evaporating DMF in the PAN-based electrospinning solution. The XRD pattern of the obtained product is similar to that of SnS@SNCF, with well

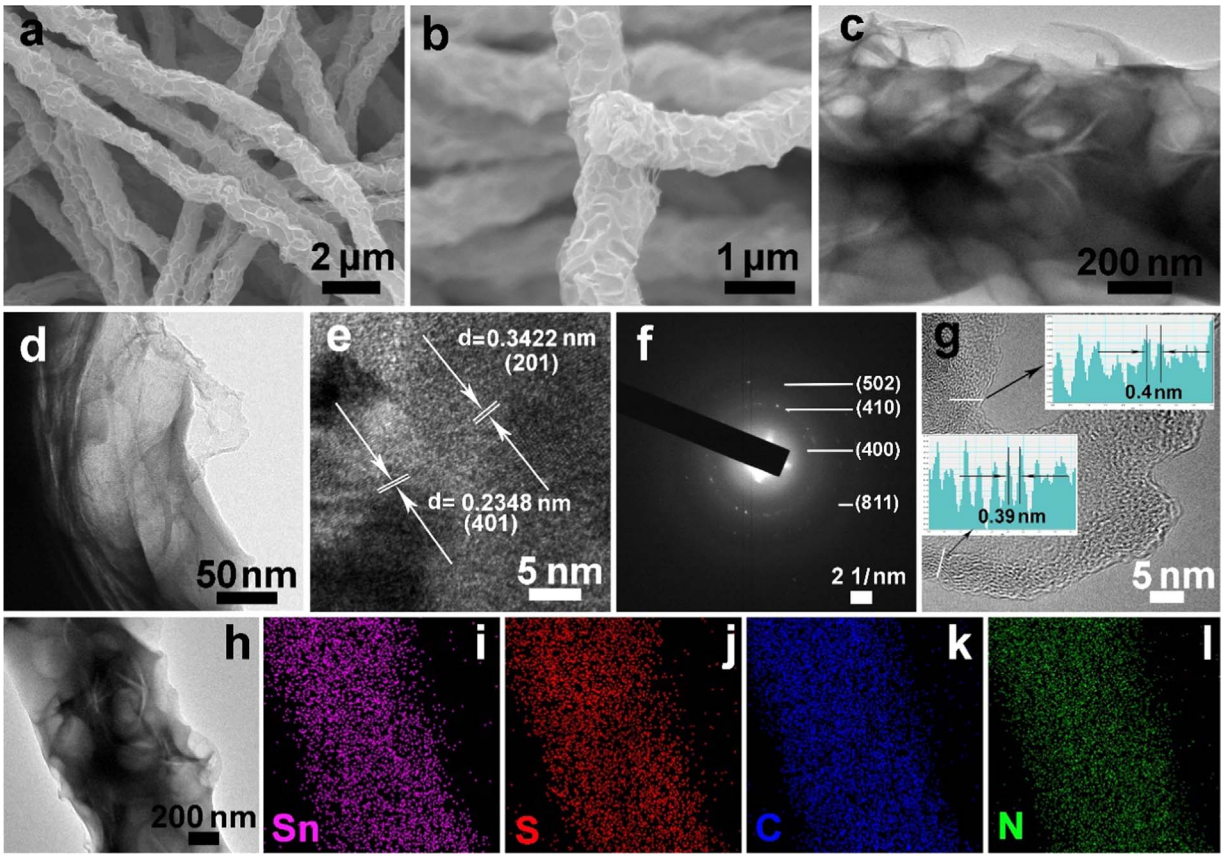

Fig. 2. SEM images (a, b), TEM images (c, d), HRTEM images (e, g), SAED pattern (f) and elemental mapping results (h–l) of SnS@SNCF-55.

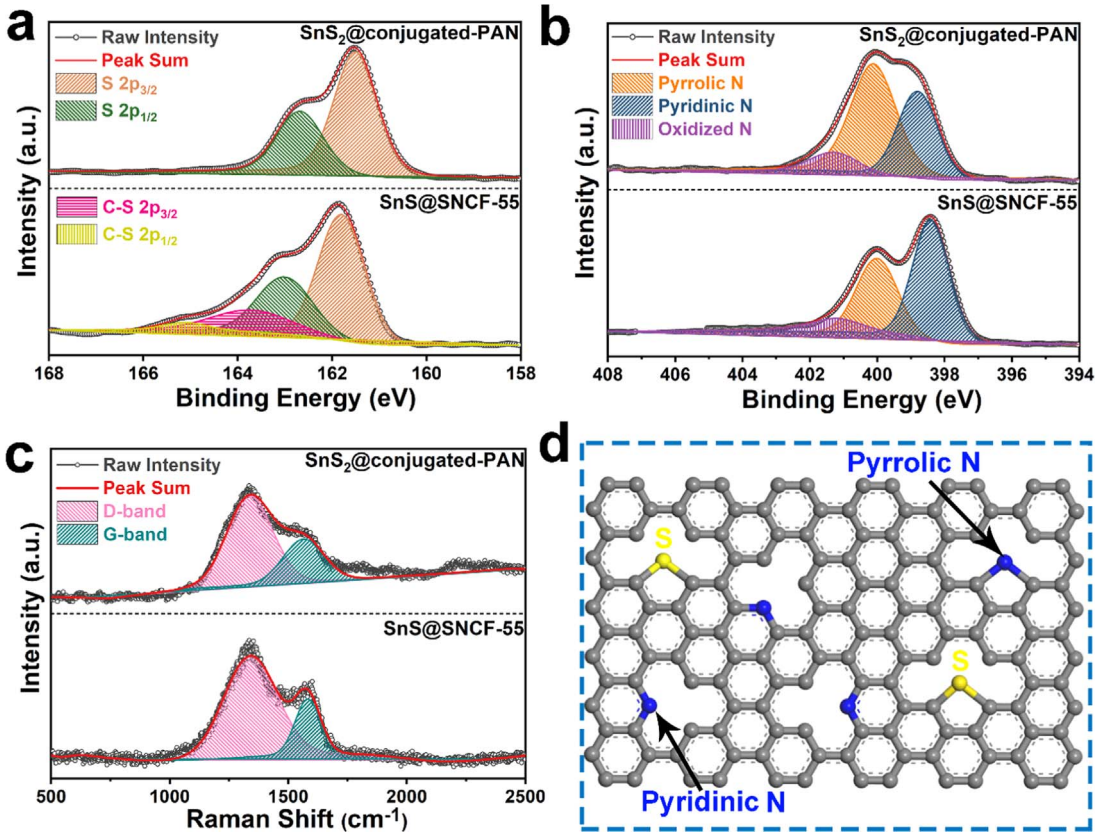

Fig. 3. (a) S 2p, (b) N 1s high-resolution XPS spectra and (c) Raman spectra of SnS_2@conjugated-PAN and SnS@SNCF-55. (d) Schematic structure of sulfur and nitrogen dual-doped carbon.

corresponded peaks for SnS and a bulged peak at around 26° for carbon (Fig. S12a), yet the morphology is very large bulk (Fig. S12b).

The chemical compositions of the products after stabilization (SnS_2@conjugated-PAN) and carbonization (sample SnS@SNCF-55) were further investigated by X-ray photoelectron spectroscopy (XPS). The survey spectra shown in Fig. S13 indicate the presence of Sn, S, C, N, O and Cl elements in SnS_2@conjugated-PAN, while the peaks for Cl are neglectable for SnS@SNCF-55, indicating some chloride impurities are removed during calcination. The C 1s high resolution XPS spectra indicate that carbon is doped with heteroatoms (Fig. S14), which can be further verified by S 2p and N 1s spectra. The S 2p spectra show a S $2p_{3/2}$ peak at 161.6 ± 0.1 eV and a S $2p_{1/2}$ peak at 163.4 ± 0.2 eV. Different from the SnS_2@conjugated-PAN precursor, the SnS@SNCF-55 sample depicts C–S bonds appeared at 163.7 and 165.1 eV in the deconvolution of S 2p spectrum, implying sulfur heteroatoms are incorporated into carbon fibers after the calcination in Ar atmosphere (Fig. 3a) [28,34–36]. Sulfidation can lead to C-C bond fission to form C-S bond for certain [37]. The high-resolution N 1s peaks in SnS_2@conjugated-PAN and SnS@SNCF-55 are also analyzed. The fitting results shown in Fig. 3b illustrate the presence of three kinds of N bonds, including pyridinic, pyrrolic and oxidized N at binding energies of 398.6 ± 0.2, 400.0 ± 0.1, and 401.1 ± 0.1 eV, respectively [17,38,39]. The content of pyrrolic N decreases along with doping S during the annealing process, which can be attributed to the preferred substitution of sulfur for pyrrolic N [26]. For the Sn 3d spectra, the binding energies are related to the valence state of tin ions (Fig. S15). SnS_2@conjugated-PAN and SnS@SNCF-55 were further examined by Raman spectroscopy. As displayed in Fig. 3c, they both display carbon characteristic peaks at around 1340 cm^{-1} (D band, implying the existence of defects) and 1580 cm^{-1} (G band, indicating the graphitic feature of carbon). The SnS@SNCF-55 shows a sharper G-band comparing with SnS_2@conjugated-PAN, demonstrating the partially graphitic structure of the carbon fibers, which is consistent with the TEM results. The schematic structure of sulfur and nitrogen dual-doped carbon is shown in Fig. 3d. Heteroatom doping induces a large number of defects in carbon fibers and creates more active sites, which can facilitate electrons and Na^+ ions transfer kinetics, increase the adsorbent ability for Na^+ ions and improve surface capacitive effects.

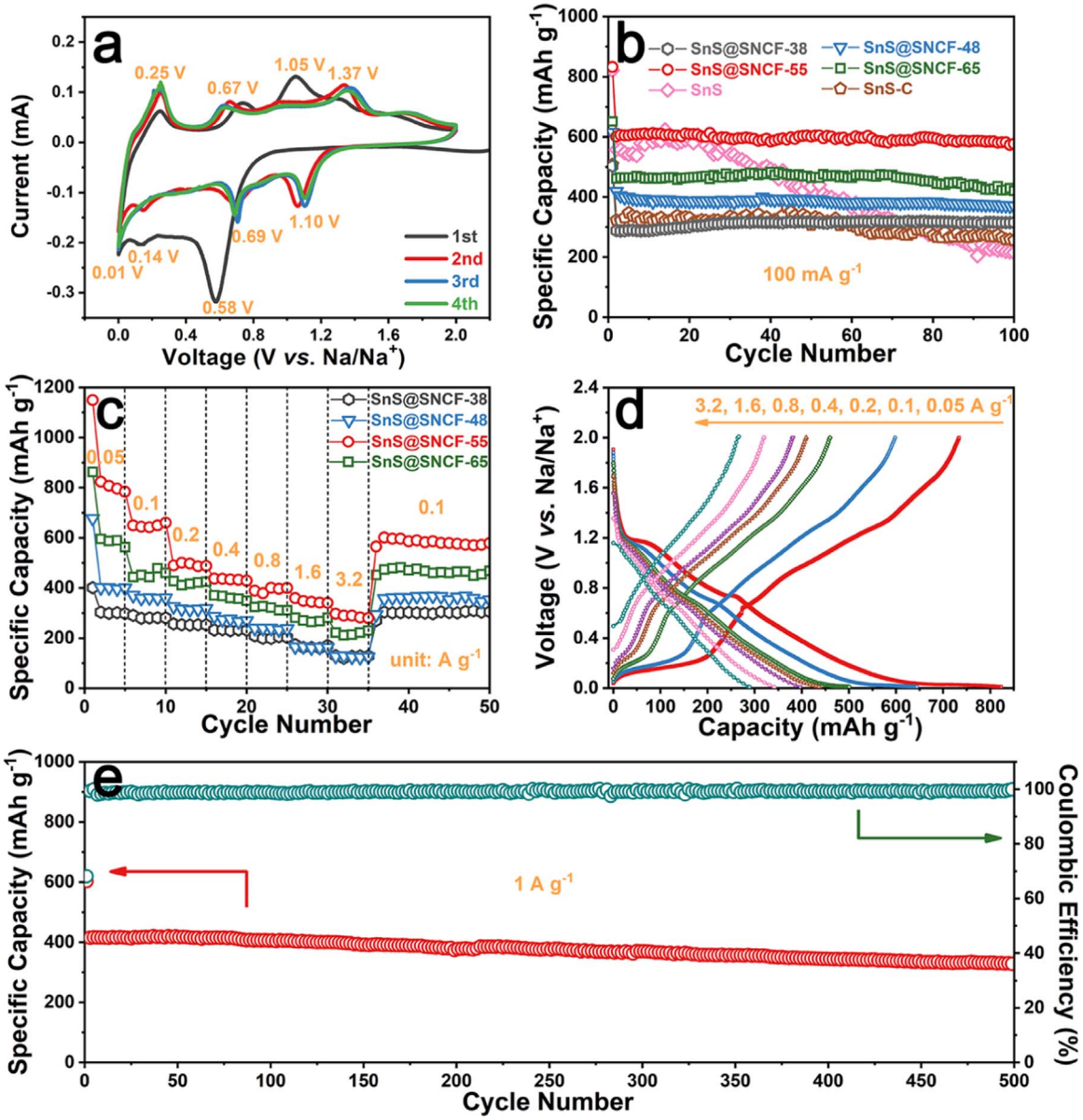

Fig. 4. (a) The initial four successive CV curves of SnS@SNCF-55 at scan rate of 0.1 mV s^{-1}. (b) Cycling performance of SnS@SNCFs, SnS and SnS-C at 100 mA g^{-1}. (c) Rate performance of SnS@SNCFs. (d) Discharge/charge profiles of SnS@SNCF-55 at different current densities. (e) Long-term cycling performance of SnS@SNCF-55 at 1 A g^{-1}.

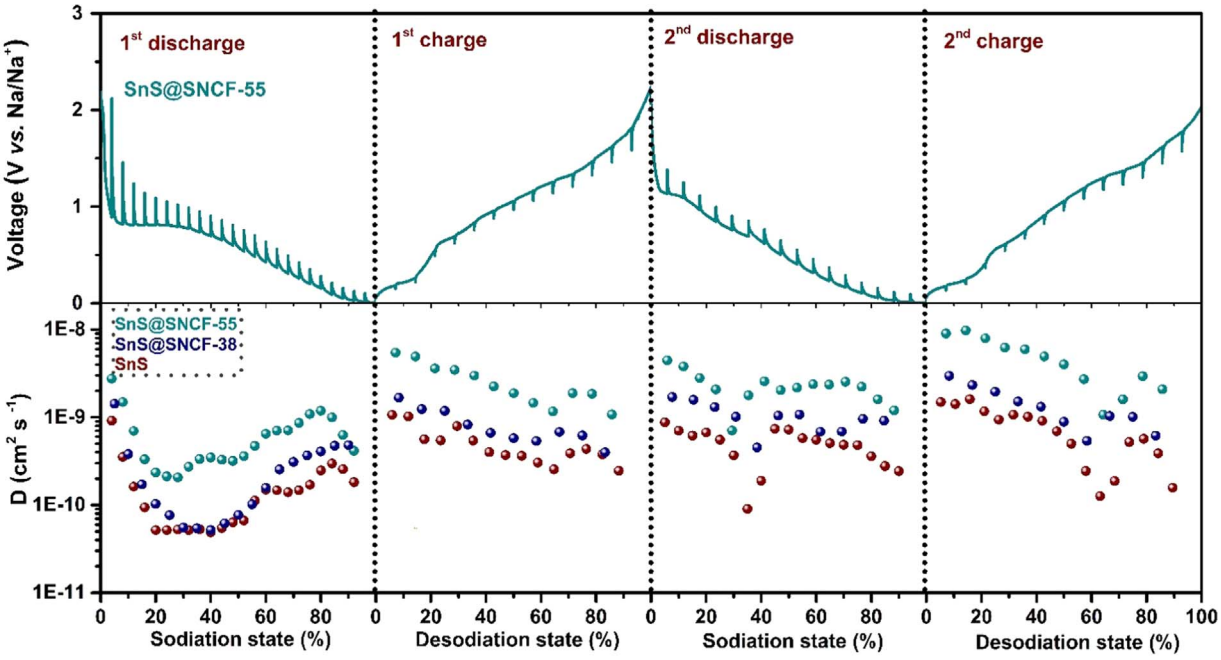

Fig. 5. GITT curves of SnS@SNCF-55 and corresponding Na^+ diffusion coefficient at different discharge/charge state.

Table 1
Electrochemical properties of Sn-based electrode for sodium ion batteries.

Electrode description	Voltage window (V)	Current density (mA g^{-1})	Specific capacity (mA h g^{-1})
Ultrasmall Sn nanoparticles embedded in carbon sphere [21]	0.01–2	200 500	493 447
SnS_2/S-rGO [34]	0.005–3	100 500	530 450
Sn-SnS-C [46]	0.01–2	100 800	485 348
SnSe/RGO [47]	0.01–2	100 500	500 430
SnSb-in-plane nanoconfined 3D N-doped porous graphene network [48]	0.005–3	100 500	400 330
SnS@rGO [49]	0.01–2	100 400	405 351
Sn_4P_3/C composite [50]	0.01–2	200 500	560 435
SnS-C microspheres [43]	0.001–3	100	540
SnS 3D flowers [41]	0.01–2	30 200	450 400
Yolk-shell Sn@C eggette-like nanostructure [51]	0.02–2	100 1000	400 200
SnS nanorods [52]	0.1–2	100 500	550 390
SnS@Graphene [14]	0–3	810	492
SnS-C [53]	0.01–2	100 400	544 493
SnO_2 nanoparticle-RGO [54]	0.005–2.5	100 1000	390 125
SnS/GO + C [55]	0.01–2	50 500	590 458
This work	**0.01–2**	**50** **100** **800**	**796** **630** **400**

The SnS@SNCFs were first assembled in half-cells to evaluate their sodium storage capability. Fig. 4a shows the first four successive CV curves of SnS@SNCF-55 electrode between 0.01 and 2 V *vs.* Na/Na^+ at a scan rate of 0.1 mV s^{-1}. In the initial scan, the cathodic peak at 0.58 V corresponds to the conversion reaction of tin sulfide to metallic tin and Na_2S, the partial alloying reaction of Sn and the formation of solid electrolyte interphase (SEI) [40,41]. The other cathodic peaks observed at 0.14 and 0.01 V can be ascribed to the multi-step alloying process of Sn and Na. The anodic peaks at 0.25 and 0.67 V correspond to the multi-step dealloying reaction of Na_xSn to Sn, while the peak at 1.05 V is related to the conversion reaction of tin to tin sulfide [38,42]. From the second scan onward, two pairs of alloying/dealloying redox peaks at 0.01/0.25 and 0.69/0.67 V, and a pair of conversion reaction peaks at 1.10/1.37 V are well overlapped, indicating the good reversibility of the SnS@SNCF anode [43].

Fig. 4b shows the cycling performances of the SnS@SNCFs at current density of 100 mA g^{-1}. The SnS@SNCF-55 sample can deliver a high capacity of 832.5 mA h g^{-1} in the first cycle and maintain a stable capacity of ~ 600 mA h g^{-1} afterwards. Both SnS@SNCF-38 and SnS@SNCF-48 show lower capacities owing to their lower contents of SnS. The SnS@SNCF-65 electrode, however, also shows lower capacity than that of SnS@SNCF-55, which can be ascribed to its large and dense SnS bulk that cannot release all capacity. In addition, the capacity of SnS@SNCF-65 starts to drop after 70 cycles, implying the inferior stability of large SnS particles for enduring the mechanical stress generated during sodiation/desodiation. The SnS-C sample also shows low and unstable capacity owing to its dense texture. For the bare SnS sample, although high capacity of ~ 580 mA h g^{-1} can be delivered, it experiences faster capacity decay after only 25 cycles. The SEM image of the SnS@SNCF-55 electrode after 100 cycles is given in Fig. S16. The fibers with good structural integrity can still be distinguished. These results demonstrate the merits of constructing a proper content of SnS nanoparticles within carbon fibers as high capacity and stable SIB anode materials.

Fig. 4c shows the rate performance of all SnS@SNCF samples. The SnS@SNCF-55 electrode can deliver specific capacities of 796, 630, 490, 433, 400, 341, and 289 mA h g^{-1} at current densities of 0.05, 0.1, 0.2, 0.4, 0.8, 1.6, and 3.2 A g^{-1}, respectively. When the current is reset to 0.1 A g^{-1}, specific capacity of 600 mA h g^{-1} can be recovered. The SnS@SNCF-55 sample exhibits better rate performance than the other three ones owing to its proper content of SnS and carbon, which is consistent with the cycling performance shown in Fig. 4b. The discharge/charge profiles of SnS@SNCF-55 at different rates are given in Fig. 4d. The plateaus observed on the discharge/charge profiles are

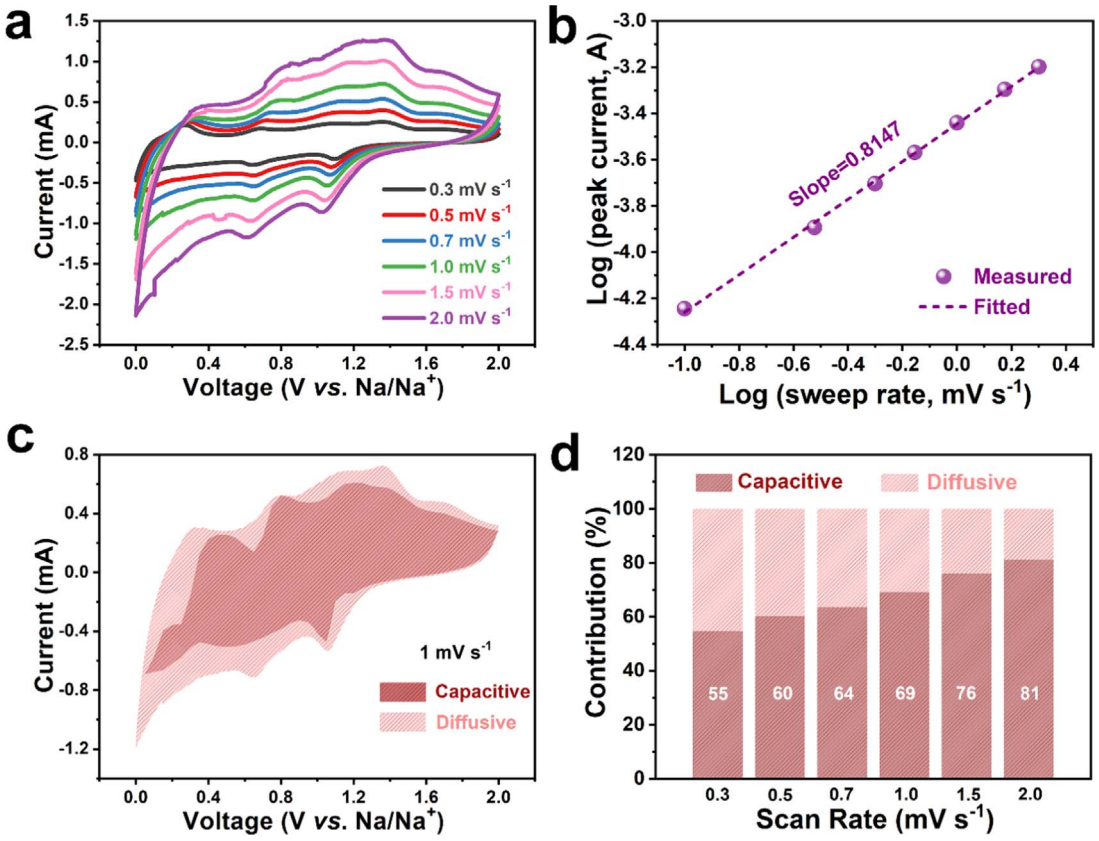

Fig. 6. (a) CV curves at different scan rates from 0.3 to 2.0 mV s^{-1}. (b) Log (peak current, A) versus log (sweep rate, mV s^{-1}) plots and the corresponding fitting line. (c) Capacitive and diffusion-controlled contribution to sodium storage of SnS@SNCF-55 at 1 mV s^{-1}. (d) Normalized contribution ratio of capacitive and diffusion-controlled capacities at different scan rates.

in good accordance with the CV curves, and experience low polarizations with the increase of current density. In Fig. 4e, long-term cycling of SnS@SNCF-55 at 1 A g^{-1} reveals its superior reversibility with high coulombic efficiency (99.2%) and a considerable capacity of 332 mA h g^{-1} after 500 cycles (capacity fading rate of 0.04% per cycle).

To further understand the improved electrochemical performance of SnS@SNCF-55, Na^+ diffusion and conductivity properties in different stages of the discharge/charge process were evaluated by galvanostatic intermittent titration technique (GITT) [44,45]. Details of the testing setup are given in the Supporting information (Fig. S17). Fig. 5 shows the GITT curves of SnS@SNCF-55 for the first two discharge/charge processes. The corresponding sodium diffusion coefficients at various sodiation/desodiation states are calculated and compared with bare SnS and SnS@SNCF-38 (Fig. S18). It can be seen that the minima values of the diffusion coefficient appear at 20–40% sodiation states or 60–80% desodiation states for all three samples, which are related to deep diffusion of Na^+ into/from the active materials. Comparing with SnS and SnS@SNCF-38, the SnS@SNCF-55 shows higher diffusion coefficients by almost an order of magnitude with much less fluctuations. The high diffusion kinetics are realized by the merits of SnS nanoparticle, that reduces the migration paths for sodium ions, and the porous carbon scaffold, that provides channels for the interpenetration of electrolytes to increase sodium ion accessibility. The bare SnS is with large particle size, while the dense carbon fiber of SnS@SNCF-38 hinders the penetration of electrolyte, which both lead to lower kinetics. The electrochemical performances of SnS@SNCF-55 and previously reported SnS or its hybrid composites are compared and summarized in Table 1, which demonstrates the superior properties of SnS@SNCF-55 as promising anode materials for sodium-ion batteries.

To probe into the electrochemical kinetics of sodium storage in SnS@SNCF-55, CV measurements at different scan rates from 0.3 to 2.0 mV s^{-1} was employed. The CV curves displayed in Fig. 6a show similar shapes at various scan rates. The contribution of capacitance or diffusion-controlled capacity can be quantified by the following relationship between peak current (i) and scan rate (v):

$$i = av^b \tag{1}$$

where both a and b are adjustable values. A b-value close to 0.5 or 1 infers that the electrochemical reaction is contributed to diffusion- or capacitive-controlled process, respectively [56,57]. The b value calculated by the slope of log (v)-log (i) plots for the cathodic peak at 1.35 V is 0.8147, suggesting the great capacity contribution from the surface-induced capacitive behavior. The ratios of capacitive contribution at different scan rates are further quantified by CV plots according to the equation [57,58]:

$$\mathrm{i}(V) = k_1 v + k_2 v^{1/2} \tag{2}$$

where k_1 and k_2 are constants for a given potential V. The $k_1 v$ stands for the capacitive-controlled contribution, while the $k_2 v^{1/2}$ for the diffusion-controlled one. Fig. 6c presents the typical voltage profile for calculated capacitive current (dark red region) in comparison with the measured current at 1 mV s^{-1}. The calculated capacitive contributions at different scan rates are displayed in Fig. 6d. The ratio of capacitive contribution enlarges along with the increase of scan rate and a high value of 81% at 2 mV s^{-1} is obtained, implying that the pseudocapacitive Na-storage contribution occupies a large amount of the whole capacity at high scan rate. This can be ascribed to the sulfur and nitrogen dual-doped mesoporous carbon fibers, which offer large surface areas and rich electroactive sites for fast capacitive sodium storage.

To further demonstrate the potential application of SnS@SNCF, a sodium-ion full-cell was assembled using SnS@SNCF-55 as anode and $Na_3V_2(PO_4)_3$ as cathode (Fig. 7a). As shown in Fig. S19, $Na_3V_2(PO_4)_3$ nanoflake arrays were successfully prepared by a one-pot, solid-state

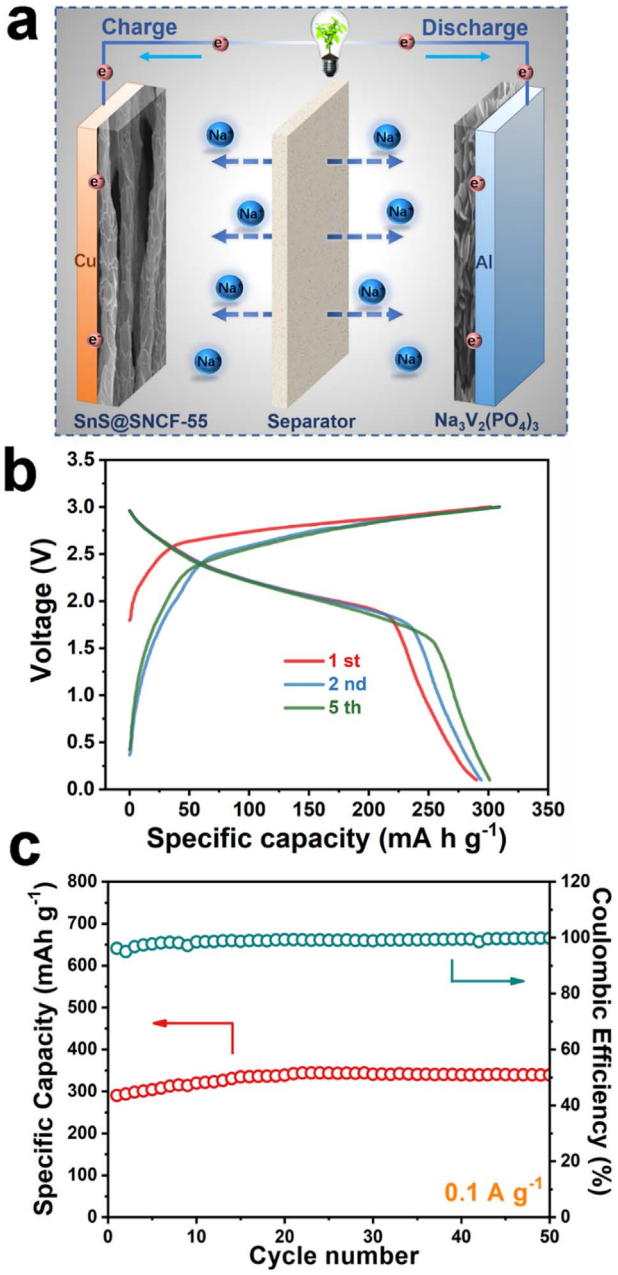

Fig. 7. (a) Schematic illustration of the $Na_3V_2(PO_4)_3$//SnS@SNCF-55 full cell configuration. (b) Charge/discharge profiles of the full cell. (c) Cycling performance of the full cell at 0.1 A g^{-1}.

reaction, with a reversible capacity of 115 mA h g^{-1} at 1 C rate (117.6 mA g^{-1}) [59]. Fig. 7b shows the charge/discharge curves of the $Na_3V_2(PO_4)_3$//SnS@SNCF-55 full cell at a current density of 0.1 A g^{-1}. It is observed that the full-cell displays a discharge plateau at about 2.2 V with a reversible capacity of about 300 mA h g^{-1} based on the weight of SnS@SNCF-55. Fig. 7c further reveals the full cell with high Coulombic efficiency (~ 99.3%) and good cycling stability with no capacity fading after 50 cycles, indicating SnS@SNCF-55 is a promising anode material for NIBs.

4. Conclusions

In summary, SnS nanoparticles embedded in sulfur and nitrogen dual-doped carbon fibers were successfully synthesized by a facile electrospinning process. A spinnable sulfur bearing solution was obtained by forming an adduct complexed with stannous chloride in DMF. This unique method introduces sulfur doping, mesopores and partially graphitic structure to the carbon fibers. A SnS@SNCF composite electrode with optimized SnS and carbon contents shows excellent electrochemical performance in both half-cell and full cell for SIBs, which can be attributed to its battery-capacitive synchronous sodium storage. The carbon-wrapped SnS nanoparticles can maintain their structural stability upon cycling to ensure high capacities, while the heteroatom doping induces abundant active sites for fast capacitive sodium storage and enhances the electronic conductivity of carbon fibers.

Acknowledgments

This work was supported by Program for New Century Excellent Talents in University (NCET-13-0594), Hunan Province Natural Science Foundation of (2018JJ1036), National Natural Science Foundation of China (Nos. 51302323, 51374255), and Innovation Project of Central South University (2017CX001).

Appendix A. Supporting information

Supplementary data associated with this article can be found in the online version at doi:10.1016/j.ensm.2018.08.014.

References

[1] J.Y. Hwang, S.T. Myung, Y.K. Sun, Chem. Soc. Rev. 46 (2017) 3529–3614.
[2] M.D. Slater, D. Kim, E. Lee, C.S. Johnson, Adv. Funct. Mater. 23 (2013) 947–958.
[3] N. Yabuuchi, K. Kubota, M. Dahbi, S. Komaba, Chem. Rev. 114 (2014) 11636–11682.
[4] D. Kundu, E. Talaie, V. Duffort, L.F. Nazar, Angew. Chem. Int. Ed. 54 (2015) 3431–3448.
[5] S.P. Ong, V.L. Chevrier, G. Hautier, A. Jain, C. Moore, S. Kim, X.H. Ma, G. Ceder, Energy Environ. Sci. 4 (2011) 3680–3688.
[6] Y. Zhao, L.P. Wang, M.T. Sougrati, Z. Feng, Y. Leconte, A. Fisher, M. Srinivasan, Z. Xu, Adv. Energy Mater. 7 (2017) 1601424.
[7] S. Qiu, L. Xiao, M.L. Sushko, K.S. Han, Y. Shao, M. Yan, X. Liang, L. Mai, J. Feng, Y. Cao, X. Ai, H. Yang, J. Liu, Adv. Energy Mater. 7 (2017) 1700403.
[8] J. Qin, N. Zhao, C. Shi, E. Liu, F. He, L. Ma, Q. Li, J. Li, C. He, J. Mater. Chem. A5 (2017) 10946–10956.
[9] N. Li, S. Liao, Y. Sun, H.W. Song, C.X. Wang, J. Mater. Chem. A 3 (2015) 5820–5828.
[10] Y. Zhang, Q. Zhou, J. Zhu, Q. Yan, S.X. Dou, W. Sun, Adv. Funct. Mater. 27 (2017) 1702317.
[11] Z. Liu, T. Lu, T. Song, X.-Y. Yu, X.W. Lou, U. Paik, Energy Environ. Sci. 10 (2017) 1576–1580.
[12] H. Hou, M. Jing, Y. Zhang, J. Chen, Z. Huang, X. Ji, J. Mater. Chem. A 3 (2015) 17549–17552.
[13] H. Ying, W.-Q. Han, Adv. Sci. 4 (2017) 1700298.
[14] T. Zhou, W.K. Pang, C. Zhang, J. Yang, Z. Chen, H.K. Liu, Z. Guo, ACS Nano 8 (2014) 8323–8333.
[15] Z. Hu, Q. Liu, S.L. Chou, S.X. Dou, Adv. Mater. 29 (2017) 1700606.
[16] D. Chao, C. Zhu, P. Yang, X. Xia, J. Liu, J. Wang, X. Fan, S.V. Savilov, J. Lin, H.J. Fan, Z.X. Shen, Nat. Commun. 7 (2016) 12122.
[17] Y. Zhang, A. Pan, L. Ding, Z. Zhou, Y. Wang, S. Niu, S. Liang, G. Cao, ACS Appl. Mater. Interfaces 9 (2017) 3624–3633.
[18] Z. Li, J. Ding, D. Mitlin, Acc. Chem. Res. 48 (2015) 1657–1665.
[19] J.M. Stratford, M. Mayo, P.K. Allan, O. Pecher, O.J. Borkiewicz, K.M. Wiaderek, K.W. Chapman, C.J. Pickard, A.J. Morris, C.P. Grey, J. Am. Chem. Soc. 139 (2017) 7273–7286.
[20] B. Zhao, Z. Wang, F. Chen, Y. Yang, Y. Gao, L. Chen, Z. Jiao, L. Cheng, Y. Jiang, ACS Appl. Mater. Interfaces 9 (2017) 1407–1415.
[21] H. Ying, S. Zhang, Z. Meng, Z. Sun, W.Q. Han, J. Mater. Chem. A 5 (2017) 8334–8342.
[22] X. Li, Y. Chen, H. Huang, Y.-W. Mai, L. Zhou, Energy Storage Mater. 5 (2016) 58–92.
[23] J. Xue, J. Xie, W. Liu, Y. Xia, Acc. Chem. Res. 50 (2017) 1976–1987.
[24] H.H. Guoqiang Zou, Ganggang Zhao, Zhaodong Huang, Peng Ge, X. Ji, Green Chem. 19 (2017) 4622–4632.
[25] F. Razmjooei, K.P. Singh, M.Y. Song, J.S. Yu, Carbon 78 (2014) 257–267.
[26] J. Yang, X. Zhou, D. Wu, X. Zhao, Z. Zhou, Adv. Mater. 29 (2017).
[27] T.J. Bandosz, T.-Z. Ren, Carbon 118 (2017) 561–577.
[28] W. Li, M. Zhou, H. Li, K. Wang, S. Cheng, K. Jiang, Energy Environ. Sci. 8 (2015) 2916–2921.
[29] R. Steudel, J. Steidel, T. Sandow, Z. Naturforsch. B 41 (1986) 951–957.
[30] C. Zhang, F. Yang, D. Zhang, X. Zhang, C. Xue, Y. Zuo, C. Li, B. Cheng, Q. Wang, RSC Adv. 5 (2015) 15940–15943.
[31] Z. Yang, J. Zhang, M.C.W. Kintner-Meyer, X. Lu, D. Choi, J.P. Lemmon, J. Liu, Chem. Rev. 111 (2011) 3577–3613.

[32] R. Alcantara, J.M. Jimenez-Mateos, P. Lavela, J.L. Tirado, Electrochem. Commun. 3 (2001) 639–642.
[33] H.L. Poh, P. Simek, Z. Sofer, M. Pumera, ACS Nano 7 (2013) 5262–5272.
[34] P. Zheng, Z. Dai, Y. Zhang, D. Khang Ngoc, Y. Zheng, H. Fan, J. Yang, R. Dangol, B. Li, Y. Zong, Q. Yan, X. Liu, Nanoscale 9 (2017) 14820–14825.
[35] C. Liu, S. Zhao, Y. Lu, Y. Chang, D. Xu, Q. Wang, Z. Dai, J. Bao, M. Han, Small 13 (2017) 1603494.
[36] Y. Guo, X. Zhang, X. Zhang, T. You, J. Mater. Chem. A 3 (2015) 15927–15934.
[37] Tae Hoon Hwang, Dae Soo Jung, Joo Seong Kim, Byung Gon Kim, J.W. Choi, Nano Lett. 13 (2013) 4532–4538.
[38] X. Xiong, C. Yang, G. Wang, Y. Lin, X. Ou, J.-H. Wang, B. Zhao, M. Liu, Z. Lin, K. Huang, Energy Environ. Sci. 10 (2017) 1757–1763.
[39] Y. Zhang, A. Pan, Y. Wang, X. Cao, Z. Zhou, T. Zhu, S. Liang, G. Cao, Energy Storage Mater. 8 (2017) 28–34.
[40] J. Wang, Y. Lu, N. Zhang, X. Xiang, J. Liang, J. Chen, RSC Adv. 6 (2016) 95805–95811.
[41] E. Cho, K. Song, M.H. Park, K.W. Nam, Y.M. Kang, Small 12 (2016) 2510–2517.
[42] J. Sheng, L. Yang, Y.-E. Zhu, F. Li, Y. Zhang, Z. Zhou, J. Mater. Chem. A5 (2017) 19745–19751.
[43] S.H. Choi, Y.C. Kang, Nano Res. 8 (2015) 1595–1603.
[44] N. Duc Tung, H.T.T. Le, C. Kim, J.Y. Lee, J.G. Fisher, I.D. Kim, C.J. Park, Energy Environ. Sci. 8 (2015) 3577–3588.
[45] X.H. Rui, N. Ding, J. Liu, C. Li, C.H. Chen, Electrochim. Acta 55 (2010) 2384–2390.
[46] L. Wu, X. Hu, J. Qian, F. Pei, F. Wu, R. Mao, X. Ai, H. Yang, Y. Cao, J. Mater. Chem. A 1 (2013) 7181–7184.
[47] X. Yang, R. Zhang, N. Chen, X. Meng, P. Yang, C. Wang, Y. Zhang, Y. Wei, G. Chen, F. Du, Chem. Eur. J 22 (2016) 1445–1451.
[48] J. Qin, T. Wang, D. Liu, E. Liu, N. Zhao, C. Shi, F. He, L. Ma, C. He, Adv. Mater. 30 (2018) 1704670.
[49] L. Wu, H.Y. Lu, L.F. Xiao, X.P. Ai, H.X. Yang, Y.L. Cao, J. Power Sources 293 (2015) 784–789.
[50] J. Qian, Y. Xiong, Y. Cao, X. Ai, H. Yang, Nano Lett. 14 (2014) 1865–1869.
[51] S. Li, Z. Wang, J. Liu, L. Yang, Y. Guo, L. Cheng, M. Lei, W. Wang, ACS Appl. Mater. Interfaces 8 (2016) 19438–19445.
[52] P.K. Dutta, U.K. Sen, S. Mitra, RSC Adv. 4 (2014) 43155–43159.
[53] L. Wu, H. Lu, L. Xiao, J. Qian, X. Ai, H. Yang, Y. Cao, J. Mater. Chem. A 2 (2014) 16424–16428.
[54] Y.X. Wang, Y.G. Lim, M.S. Park, S.L. Chou, J.H. Kim, H.K. Liu, S.X. Dou, Y.J. Kim, J. Mater. Chem. A 2 (2014) 529–534.
[55] Y.C. Lu, C. Ma, J. Alvarado, N. Dimov, Y.S. Meng, S. Okada, J. Mater. Chem. A 3 (2015) 16971–16977.
[56] V. Augustyn, P. Simon, B. Dunn, Energy Environ. Sci. 7 (2014) 1597–1614.
[57] J. Wang, J. Polleux, J. Lim, B. Dunn, J. Phys. Chem. C 111 (2007) 14925–14931.
[58] D. Chao, P. Liang, Z. Chen, L. Bai, H. Shen, X. Liu, X. Xia, Y. Zhao, S.V. Savilov, J. Lin, Z.X. Shen, ACS Nano 10 (2016) 10211–10219.
[59] X. Cao, A. Pan, S. Liu, J. Zhou, S. Li, G. Cao, J. Liu, S. Liang, Adv. Energy Mater. (2017) 1700797.